The Cryosphere
Discussions
Open Access
EGU

# Debris cover and the thinning of Kennicott Glacier, Alaska, Part B: ice cliff delineation and distributed melt estimates

5    Leif S. Anderson[1,2], William H. Armstrong[1,3], Robert S. Anderson[1], and Pascal Buri[4]

[1]Department of Geological Sciences and Institute of Arctic and Alpine Research, University of Colorado Campus Box 450, Boulder, CO 80309, USA
[2]GFZ German Research Centre for Geosciences, Telegrafenberg, 14473 Potsdam, Germany
10    [3]Department of Geological and Environmental Sciences, Appalachian State University,033 Rankin Science West, ASU Box 32067, Boone, NC 28608-2067, USA
[4]Geophysical Institute, University of Alaska-Fairbanks, 2156 Koyukuk Drive, Fairbanks, AK 99775, USA

15    *Correspondence to*: Leif Anderson (leif@gfz-potsdam.de)

**Abstract.** The mass balance of many valley glaciers is enhanced by the presence of ice cliffs within otherwise continuous debris cover. We assess the effect of debris and ice cliffs on the thinning of Kennicott Glacier in three companion papers. In Part A we report in situ measurements from the debris-covered tongue. Here, in Part B, we develop a method to delineate
20    ice cliffs using high-resolution imagery and use empirical relationships from Part A to produce distributed mass balance estimates. In Part C we describe feedbacks that contribute to rapid thinning under thick debris.

Ice cliffs cover 11.7% of the debris-covered tongue, the most of any glacier studied to date, and they contribute 19% of total melt. Ice cliffs contribute an increasing percentage of melt the thicker the debris cover. In the lowest 4 km of the glacier, where debris thicknesses are greater than 20 cm, ice cliffs contribute 40 % of total melt.

25    Surface lake coverage doubled between 1957 and 2009, but lakes do not occur across the full extent of the zone of maximum glacier thinning. Despite abundant ice cliffs and expanding surface lakes, average melt rates are suppressed by debris, the pattern of which appears to reflect the debris thickness-melt relationship (or Østrem's curve). This suggests that, in addition to melt hotspots, the decline in ice discharge from upglacier is an important contributor to the thinning of Kennicott glacier under thick debris.

30    **Keywords:** mass balance; lake; WorldView; Østrem's curve; backwasting

## 1 Introduction

Thick debris insulates ice and reduces melt rates. But debris-covered glaciers often respond to climate change in ways that
35    appear contradictory to this melt-suppressing effect. In High Mountain Asia (*HMA*) many debris-covered and debris-free glacier tongues are thinning at similar rates (e.g., Kääb et al., 2012; Brun et al., 2018). This apparent paradox is known as the 'debris-cover anomaly' (Pellicciotti et al., 2015), and has been documented in *HMA* and the European Alps (Nuimura et al., 2012; Pellicciotti et al., 2015; Agarwal et al., 2017; Lamsal et al., 2017; Wu et al., 2018; Mölg et al., 2019). But the debris-cover anomaly also occurs on glaciers in the Wrangell Mountains of southern Alaska (Das et al., 2014 ).

40    Kennicott Glacier is the largest glacier in the Wrangell Mountains with debris cover that extends continuously across its width. As shown in Figures 1 and 2, the maximum surface elevation change on Kennicott Glacier occurs under thick debris.

1

Greater surface elevation changes are documented from the Kennicott debris-covered tongue than from any portion of the largely debris-free Nabesna Glacier, north of Kennicott Glacier (Supplemental Figure 1; Das et al., 2014). It is not clear why the greatest thinning of Kennicott Glacier occurs under thick debris and at rates similar to nearby debris-free glaciers. We

45  define a zone of maximum thinning or *ZMT* under debris cover where the glacier thinned at an average rate greater than 1.4 m yr$^{-1}$ between 1957 and 2009 (Fig. 1; Das et al., 2014). For Kennicott Glacier, thinning rates this high only occur near the terminus under thick debris (Fig. 2). The *ZMT* occupies a 2-km down-glacier by 3.5-km across-glacier portion of the debris-covered tongue.

The debris-cover anomaly can be explained by constraining the individual components of the continuity equation for ice

50  from glacier ablation zones:

$$\frac{dH}{dt} = \dot{b} - \frac{dQ}{dx} - \frac{dQ}{dy} \quad ,$$ (1)

where $H$ is the ice thickness, $t$ is time, $\dot{b}$ is the annual specific ablation (or loosely ice melt in the ablation zone), and $Q$ is the column integrated ice discharge (or loosely ice dynamics) (Fig. 3). Constraining $\dot{b}$ is particularly difficult due to the presence of ice cliffs, lakes, and streams on debris-covered glacier surfaces. The annual specific balance in the ablation

55  zone can be sub-divided,

$$\dot{b} = \dot{b}_s + \dot{b}_e + \dot{b}_b$$ (2)

where $\dot{b}_s$ is the annual surface ablation, $\dot{b}_e$ is the annual englacial ablation, and $\dot{b}_b$ is the annual basal ablation rate. Surface ablation typically dominates $\dot{b}$ in most glacial settings and it is not yet possible, to quantify $\dot{b}_e$ or $\dot{b}_b$ within and under debris-covered glacier tongues. Building from Eq. (1), $\dot{b}_s$ is negative in the ablation zone, and therefore

60  shifts $\frac{dH}{dt}$ towards negative values, thinning the glacier. In the ablation zone, the sum of $\frac{-dQ}{dx} - \frac{dQ}{dy}$ tends to be positive, because more ice typically flows into a fixed planview area than leaves it leading to surface uplift. This ice emergence velocity counters surface lowering caused by melt.

Two common explanations for the debris-cover anomaly follow from Eq. (1) ( Immerzeel et al., 2014; Vincent et al., 2016; Brun et al., 2018). First, it is possible that ablation within debris-covered areas is higher than we expect, causing thinning. In

65  this case, $\dot{b}$, averaged across the glacier, is more negative than what insulated, sub-debris ablation rates suggest. Local *melt hotspots* such as ice cliffs, lakes, streams, and thermokarst counter the insulating effects of debris (e.g., Kirkbride, 1993; Sakai et al., 2002; Reid and Brock, 2014; Miles et al., 2018). In addition, lakes can enhance melt on debris-covered glaciers by an order of magnitude compared to proximal sub-debris melt (e.g., Immerzeel et al., 2014).

Second, thinning upglacier of the thick debris cover leads to reduced ice flow to the debris-covered tongue, leading to a less

70    positive   $\dfrac{-dQ}{dx} - \dfrac{dQ}{dy}$   , reduced ice emergence rates, and glacier thinning (e.g., Nye, 1960; Vincent et al., 2016; Brun et al., 2018).

On Kennicott Glacier thousands of ice cliffs are scattered within the otherwise continuous debris cover. These abundant ice cliffs will increase area-averaged melt rates and counteract the insulating effect of debris. Debris thicknesses on Kennicott Glacier are typically less than 50 cm (Part A) reducing the insulating effect of debris relative to many other previously-

75    studied glaciers. If melt hotspots control the location of the *ZMT* then we should expect their effect to be maximized in the *ZMT*. But if melt hotspots are not dominant then we should expect the mass balance profile to be dictated by the debris-thickness melt relationship (or Østrem's curve ) downglacier (e.g., Anderson and Anderson, 2018). We therefore address: *What is the mass balance profile within the debris-covered tongue of Kennicott Glacier?* And *do melt hotspots within debris cover maximize glacier-wide melt in the location of maximum glacier-wide thinning (or ZMT)?*

80    To address these questions, we quantify the role of ice cliffs and sub-debris melt across the debris-covered tongue. In Part A, we show that sub-debris melt rates tend to decrease downglacier as debris thickness increases. Mean ice cliff backwasting rates, on the other hand, increase downglacier. In order to determine the mass balance pattern within the debris cover, ice cliff distribution must be quantified. We therefore present 1) a new method for remotely delineating ice cliffs using high-resolution WorldView 1 images; 2) estimates of the ice cliff distribution; and 3) combined estimates of ice cliff

85    and sub-debris melt across the study area. In order to assess if surface lakes control the location of the *ZMT* we also digitized surface lake extent in 1957 and 2009.

## 1.1 Study glacier

Kennicott Glacier is a broadly south-southeast facing glacier located in the Wrangell Mountains, Alaska (Fig. 1; 42 km long; 387 km² area). As of 2015, 20% of Kennicott Glacier was debris-covered. Below the equilibrium-line altitude at about

90    1500 m (Armstrong et al., 2017), 11 medial moraines (e.g., Anderson, 2000) can be identified on the glacier surface. Above 700 m elevation debris is typically less than 5 cm thick, although, locally, areas with low surface velocities tend to have thicker debris (Anderson and Anderson, 2018). Medial moraines coalesce 7 km from the terminus to form a debris mantle with ice cliffs, streams, and lakes scattered within an otherwise continuous debris cover. The first sinkhole lakes and collapse features are documented in aerial imagery from 1937 within 400 meters of the terminus (Rickman and Rosenkrans,

95    1997). As surface slopes have lowered in the lowest four kilometers of the glacier, thermokarst collapse features and surface lakes have expanded upglacier (Rickman and Rosenkrans, 1997).

## 2 Methods

The presence of ice cliffs and surface lakes on debris-covered glaciers partially makes distributed estimates of mass balance difficult. The extent of melt hotspots must be defined to make distributed melt estimates. A new method for the detection of

100    ice cliffs has been developed using high-resolution digital elevation models (DEMs) with 5-meter resolution (Herreid and Pelliccotti, 2018). Despite the efforts of projects like the ArcticDEM (Porter et al., 2018), glacier coverage with high resolution DEMs is still rarer than coverage with orthoimagery. Here we introduce a new method to delineate ice cliffs

3

using solely high-resolution satellite imagery. We use this method to delineate ice cliffs on the surface of Kennicott Glacier.
Using the delineated ice cliffs and the in situ measurements described in Part A and shown in Figure 4, we estimate ice cliff
105    and sub-debris melt across the debris-covered tongue.

## 2.1 Remote sensing methods

We describe an automated algorithm to delineate ice cliffs from optical satellite imagery. We use 0.5 m resolution
WorldView (WV) satellite imagery acquired on 13 July 2009 (catalog ID: 1020010008B20800) to delineate ice cliffs across
the study area. The 2009 WV image was the closest high-resolution image available in time to the 2011 summer field
110    campaign. We used WV stereoimagery from 2013 to produce glacier surface DEMs at 5 m spatial resolution using the
Ames Stereo Pipeline (Shean et al., 2016), which we use to represent the glacier surface in 2011.

### 2.1.1 Automated ice cliff detection methods

Our method for detecting ice cliffs relies on the observation that ice cliffs are generally darker than the debris around them.
Ice cliffs are typically coated with a thin, wet debris film, which appears darker than the adjacent, dry debris in
115    panchromatic optical imagery (Fig. 5). In addition, steep ice cliffs are often more shaded than nearby lower-sloped debris-
covered surfaces.

The workflow we outline relies on open-source Python packages, which facilitates the method's replication and
improvement by other researchers. Our workflow consists of three general steps: 1) stretching the image brightness
histogram to a suitable range for our ice cliff detection methods; 2) applying an ice cliff detection method; and 3)
120    morphologically filtering of the detected ice cliffs (Fig. 5).

We use two methods to detect ice cliffs: i) the adaptive binary threshold method (*ABT*; skimage.filters.adpative_threshold
tool; e.g., Sauvola and Pietikäinen, 2000); and ii) the Sobel edge detection method (*SED*; skimage.filters.sobel tool;
Richards, 2013). We use separate saturation stretches (Fig. 5) for each method by applying the exposure function in the
scikit-image package (skimage).

125    The *ABT* approach runs a moving window over the image, calculates the mean brightness value within that window, and
then uses a threshold to binarize the image. Because the brightness threshold varies across the image, the *ABT* approach is
insensitive to changes in illumination and debris color.

The *SED* approach estimates spatial gradients in image brightness. The Sobel operator detects high contrasts between light-
colored debris and dark-colored ice cliffs. The saturation stretch applied on the orthoimage causes dark ice cliffs to appear
130    as featureless black regions, which the Sobel operator returns as low gradient values. We apply a brightness gradient
threshold to isolate ice cliffs.

Both detection methods (*ABT* and *SED*) produce false positives from shaded, over-exposed, or textureless debris cover
(*SED* only). The *SED* approach produces many false positives, which generally have a characteristic speckled appearance,
and often occur in small, isolated groups. We apply morphological opening (Dougherty, 1992) to remove these isolated,
135    distributed false positives (skimage.morphology.opening; Fig. 5). In addition, the *SED* approach creates false positives in

4

regions that have been over-exposed by the saturation stretch and therefore lack texture. We remove these *SED* false positives by masking pixels with the maximum brightness.

To maximize correct ice cliff identification and minimize false positives we compare our ice cliff estimates to hand-digitized ice cliffs from twelve 90,000 m$^2$ regions. The cumulative area used in the error checks was 1.8 km$^2$, approximately
140   7.4% of the 24.2 km$^2$ study area (Fig. 6). There is some operator subjectivity in delineating ice cliffs from satellite imagery, especially for smaller ice cliffs. To minimize this issue, two different human operators independently delineated ice cliffs. As these independent delineations agreed within 3% in their ice cliff area, we consider operator misidentification to be a negligible source of error.

Seven parameters determine the success of these ice cliff detection methods: i-ii) the low and high end brightness values
145   used for the saturation stretch; iii-iv) the window size and offset from mean brightness in the *ABT* method, v) the high-end value to use for thresholding in the *SED* method, and; vi-vii) the kernel sizes used in morphological filtering of the *SED* and *ABT* results. To find the best parameter set we use a Monte Carlo approach for multi-objective optimization (Yapo et al., 1998). We ran the ice cliff detection algorithm 2500 times, while varying parameters sampled from uniform distributions (Duan et al., 1992). We evaluate algorithm performance by comparing ice cliff area from the automated routine against the
150   hand-digitized ice cliff areas. Our optimization simultaneously seeks to maximize true positive ice cliff detection, while minimizing false positives and false negatives. We manually inspect the top-performing parameter sets, ranked by Euclidean distance from the origin, which defines perfect algorithm performance (Fig. 7; Reed et al., 2013). We chose image processing parameters slightly off the set with the smallest euclidean distance to reduce false positives (Table 1).

### 2.2 Distributed estimates of melt

155   Previous studies have estimated ice cliff backwasting rates as they vary in space using DEM-differencing, models, and in situ measurements. These approaches have shown that 1) ice cliff survivability varies strongly with aspect at lower latitude (Sakai et al., 2002; Buri and Pellicciotti, 2018); 2) ice cliff backwasting is highly sensitive to cliff slope (Reid and Brock, 2014); 3) local topography plays an important role in local ice cliff backwasting rates (Steiner et al., 2015; Part A); and 4) lakes allow for the long-term persistence of ice cliffs (Watson et al., 2017). Although, we lack detailed on-glacier
160   meteorological data, on the Kennicott Glacier, we take advantage of a rich dataset of in-situ backwasting measurements from 60 ice cliffs (Part A). We use an alternative approach to distributed melt estimation by extrapolating our in situ measurements across the debris-covered tongue.

We extrapolate the empirical measurements from Part A (Fig. 4) across the study area. We use empirical curve fits of debris thickness as it varies with elevation, sub-debris melt as it varies with debris thickness, and ice cliff backwasting as it varies
165   with elevation to distribute our measurements across the study area. These estimates are meant to represent the period from 18 June to 16 August 2011 (Part A).

The summer specific mass balance $\dot{b}_s$ is divided into contributions from sub-debris and ice cliff melt: $\dot{b}_{debris}$ and

$\dot{b}_{icecliff}$. Each 1 m pixel is designated as debris or ice cliff using the *ABT* ice cliff delineation method. We use the *ABT* method because it consistently performs better than the *SED* method (see Results section). For the most-likely case we

5

170     apply a bias correction by adding 20% to the ice cliff area in each elevation band based on the consistent underprediction of
        ice cliffs.

        We extrapolate debris thickness across the study area by applying the elevation dependent curve to all debris-designated
        pixels. Debris thickness $h_{debris}$ varies with elevation $z$ according to:

$$h_{debris} = \frac{a}{\left[1 + 10^{\frac{(z-b)}{100}}\right]} + c \quad , \quad (3)$$

175

        where the fitted parameters $a$, $b$, and $c$ have values of 25.7 cm, 571 m, and -0.24 cm, respectively.

        We apply sub-debris melt-debris thickness relationship to all debris-designated pixels. The relationship between specific
        sub-debris melt $\dot{b}_{debris}$ and debris thickness is:

$$\dot{b}_{debris} = \dot{b}_{ice} \frac{h_{star}}{(h_{debris} + h_{star})} \quad , \quad (4)$$

180     where $\dot{b}_{ice}$, the bare-ice melt rate measured near the top of the study area, and $h_{star}$ have values of 5.87 cm d⁻¹ and 8.17
        cm respectively. The hyperbolic fit between debris thickness and sub-debris melt assumes that energy is transferred through
        the debris by conduction (see Anderson and Anderson, 2016).

        We then apply the ice cliff backwasting-elevation relationship to all ice cliff pixels. Based on the results from Part A, we
        ignore ice cliff backwasting variation with orientation. We fit a linear-relationship between elevation $z$ and specific
185     horizontal ice cliff retreat:

$$\dot{b}_{backwasting} = f * z + g \quad , \quad (5)$$

        where the fitted parameters $f$ and $g$ are -0.0123 cm (m d)⁻¹ and 13.94 cm d⁻¹, respectively. In Part A we did not find a
        significant difference between backwasting for ice cliffs with and without lakes at their base. Because the backwasting rate
        is measured horizontally, we apply an average dip relative to the horizontal plane ($\theta$) to estimate the melt perpendicular to
190     the ice cliff surface:

$$\dot{b}_{icecliff} = \dot{b}_{backwasting} \cos(90 - \theta) \quad (6)$$

        In the most-likely case we assume a uniform ice cliff slope ($\theta$) for all ice cliffs of 40° based on an analysis of 2m-
        ArcticDEMs (Porter et al., 2018) over several seasons.

        In order to estimate the mass balance with elevation we integrate the contributions of ice cliff and sub-debris ablation across
195     50 meter elevation bands:

6

$$\bar{b}^i = \frac{\displaystyle\iint^{A^i_{debris}} \dot{b}_{debris}\, dx\, dy + \iint^{A^i_{icecliff}} \dot{b}_{icecliff}\, dx\, dy}{A^i} \quad (7)$$

where $\bar{b}^i$ is the mean ablation rate within the elevation band $i$ in units of m d$^{-1}$, $A^i_{debris}$ is the total debris-covered area within the elevation band, $A^i_{icecliff}$ is the total ice cliff area within the elevation band, $A^i$ is the total area within the elevation band ,and $dx$ and $dy$ are both 1 m.

We present one most-likely distributed empirical melt estimate, which we bound with two extreme cases. For the most-likely case the curve fits are calculated using the median of data from the 50-m elevation bins (Fig. 4). See Table 2 for the extreme parameters used for the distributed melt estimates. In the extreme cases for the debris thickness and ice cliff backwasting, curve fits were made through the 25% and 75% data points in each elevation bin (Fig. 4; Supplemental Figure 2).

**2.3 Modeled bare-ice melt rates across the study area**

For reference we also estimate the bare-ice melt rate through the study area for the summer of 2011, in the hypothetical case that no debris was present on the glacier. We calculate the bare-ice melt factor from several ablation stakes in bare-ice in the northeastern portion of the study area (Part A). We calculate the melt factor for ice (e.g., Hock, 2003) $MF_{ice}$ using measured bare-ice ablation ( $\dot{b}_{ice}$ ) and air temperatures interpolated across the glacier:

$$MF_{ice} = \frac{\displaystyle\sum_{i=1}^{n} \dot{b}_{ice}}{\displaystyle\sum_{i=1}^{n} T^+ \Delta t} \quad . \qquad (8)$$

where $T^+$ is the positive degree-days defined as the mean daily air temperature when above 0° C and $\Delta t$ is one day. Air temperatures did not drop below freezing during the study period. We use hourly air temperature data from the Gates Glacier and May Creek meteorological stations to estimate the $T^+$ at each measurement location. Gates Glacier station is located off-glacier at 1240 m elevation and May Creek station is located at an elevation of 490 m located 15 km to the southwest of the town McCarthy (Fig. 1).

**2.4 Digitization of surface lakes from 1957 and 2009**

In order to compare the extent of surface lakes with the *ZMT* we hand-digitized lakes from the 1957 and 2009 summer images. Lakes were searched for using a fixed grid to insure complete coverage of the study area. Digitized lake extents were confirmed by independent operators. Depressions on the glacier surface with exposed ice and/or ice-cut shorelines were digitized and assumed to be former lakes that subsequently drained.

**3 Results**

**3.1 Remotely-sensed ice cliff extent**

7

### 3.1.1 Performance of ice cliff detection methods

225  The adaptive binary threshold (*ABT*) method outperforms the Sobel edge detection (*SED*) method. Averaged across the error checks, the *ABT* method correctly identifies 58% of ice cliff area, with 21% false positives. Percentages are relative to the hand-digitized ice cliff areas. The *SED* method yields a lower percentage of correctly identified ice cliffs (45%), but also produces fewer false positives (14%). In regions where we do not have manually digitized ice cliffs, our estimates of ice cliff area represent both true and false positives. Assuming our success rate is consistent across the glacier, we expect the

230  *ABT* and *SED* approaches to detect 79% and 69% of the true ice cliff area, respectively.

Some systematic errors are evident, as anomalously light and dark regions of the glacier produce higher error. Regions of thin debris are especially problematic when using the *SED* method (Fig. 6; see also Herreid and Pellicciotti, 2018 ). To correct for this error in the *SED* results, where debris is very thin, we manually removed areas with highly erroneous ice cliff detections; these only occur at higher elevations in the study area (Fig. 6). Due to its poorer performance, we do not use

235  the *SED*-defined ice cliff area for the distributed mass balance estimates.

### 3.1.2 Spatial distribution of ice cliffs

The two detection methods produce broadly similar ice cliff distributions. The *SED* method, specifically, overestimates ice cliff area at high elevation due to the thin, dark-colored debris. Over the 24.2 km$^2$ study area, we estimate that ice cliffs cover 2.14 km$^2$ (8.8%) and 2.32 km$^2$ (9.7%) of ice cliff planview area using the *SED* and *ABT* methods, respectively (Fig.

240  8). If we apply a bias correction to the *SED* (30%) and *ABT* (20%) estimates based upon under-detection rates in manually digitized areas, the ice cliffs cover 11.4% and 11.7% of the glacier respectively. Focusing on the *ABT* results, which provide the most accurate estimate, we find a "humped" profile in the elevational distribution of ice cliff area. Ice cliff area peaks between 600 and 620 m a.s.l. Below this elevation, ice cliff area decreases (Fig. 8).

In total, 11.6 % of the debris-covered tongue of Kennicott glacier is occupied by ice cliffs. This is 60% more coverage by

245  percentage than on the Changri Nup Glacier, the glacier with the second highest coverage of ice cliffs studied to date (Table 3). The Kennicott Glacier has the lowest mean debris thickness (13 cm) of glaciers with reported ice cliff coverage percentages and supports the highest percentage of ice cliffs. This implies that ice cliff coverage varies with debris thickness.

We normalized ice cliff area by glacierized area within each elevation band, which we refer to as ice cliff fractional area. Ice

250  cliff fractional area is relatively uniform at 7-8% except for a broad peak between 500-660 m elevation within which fractional area reaches 13% at 540-560 m. The lower edge of this peak overlaps with the upper end of the *ZMT* (see Part C for further discussion).

### 3.2 Distributed estimates of melt

In Figure 9 we show the distributed estimates of melt split into sub-debris and ice cliff contributions across the study area.

255  While sub-debris melt decreases toward the terminus due to thickening debris, ice cliff backwasting rates increase toward the terminus due to increasing energy available for melt.

8

When averaged across the entire study area, 81% of mass loss is expected to come from sub-debris melt and 19% from ice cliff melt. Maximum bounds for the total contribution of ice cliffs to mass loss are 12% and 28%. Figure 10 shows that the insulating effects of debris cover dominates the melt-enhancing effect of ice cliffs when averaged across elevation bands.

260 Modeled bare ice melt rates, which are meant to represent the hypothetical melt rate if debris were absent from the study area, increase towards lower elevations and range from -5.9 to -7 cm d$^{-1}$ (Fig. 10). The dominance of decreasing sub-debris melt downglacier, due to thickening debris, results in a sharp deviation from the bare-ice melt rate near 700 m elevation (relative to the 2015 glacier surface). Elevation-band averaged sub-debris melt rates decline from 5.7 cm d$^{-1}$ at the top of the study area to 1.6 cm d$^{-1}$ near the terminus.

265 Ice cliffs produce mean elevation-band averaged melt rates of 0.33 cm d$^{-1}$ at the top of the study area and 0.78 cm d$^{-1}$ near the terminus. The maximum contribution of ice cliffs to band-averaged melt occurs near 500 m and has a value of 1.1 cm d$^{-1}$. Ice cliffs contribute most to mass loss in the 500 to 520 m elevation band, close to where the ice cliff fractional area also maximizes. Across all of the elevation bands, the ice cliffs between 500 and 520 m generate a maximum of 40% of the total mass loss due to ice cliffs and sub-debris melt.

270 **3.3 Surface lake coverage**

In 1957, lakes would have covered only 0.4 % of the study area. By 2009, surface lakes had expanded upglacier and more than doubled their surface area compared to the 1957 image, covering 0.94% of the study area. Lakes occupied 2.0% of the portion of the glacier with 4 km of the terminus and 0.39% of the upper portion of the study area in 2009. In both the 1957 and 2009 images lake coverage is almost zero in the upper portion of the zone of maximum thinning (Fig. 10).

275

**4 Discussion**

**4.1 Ice cliff detection methods**

Our automated methods provide an accurate estimate of ice cliff area, though both the *ABT* and *SED* ice cliff detection methods underpredict ice cliff area, without bias corrections. These methods require that ice cliffs are dark relative to

280 surrounding debris cover. Ice cliffs may be brighter than the surrounding debris if the ice cliffs are not covered with thin debris films or if they are strongly illuminated. Our method will therefore likely underpredict south-facing ice cliffs, although we observe many correct detections.

Future improvements to these detection methods may be achieved using more advanced image segmentation techniques (e.g., Leyk and Boesch, 2010), by utilizing image texture analysis, or by adaptively changing image processing parameters

285 within a window moving across the image and mosaicing the results. Using multispectral imagery would also likely improve detection, although such imagery is less readily available. The detection methods presented here could be compared to the cliff delineation algorithm of Herreid and Pellicciotti (2018) using existing high-resolution DEMs.

**4.2 Distributed estimates of melt**

On Kennicott Glacier, ice cliffs most likely contribute 19% of volume loss of the debris-covered tongue. This percentage is

290 more than twice the percentages reported from other glaciers with mean debris thicknesses less than 50 cm (Table 3). This is

9

The Cryosphere
Discussions
EGU
Open Access

likely due to the high fractional coverage of ice cliffs on the Kennicott Glacier. For glaciers with mean debris thicknesses much larger than 50 cm, ice cliff contributions are larger than 19% and reach 40%. These high ice cliff contributions occur despite much lower ice cliff coverage when compared to Kennicott Glacier (Table 3).

295    Ice cliffs tend to contribute a higher fraction of mass loss as debris thickness increases. This trend is visible on Kennicott Glacier as debris thickens toward the terminus (Fig. 10). This relationship also appears to hold when considering debris-covered glaciers from different regions (Table 3). As debris thickens the contribution of ice cliff melt also tends to increase. This appears to occur even though the fractional coverage of ice cliffs tends to decrease as mean debris thicknesses increase.

Ice cliffs do not counteract the insulating effects of debris on Kennicott Glacier (Figs. 10 and 11). Thin debris leads to melt rates closer to bare-ice melt rates. Kennicott Glacier also has the highest fractional coverage of ice cliffs, relative to other
300    studied glaciers, which serves to increase melt rates (Table 3). Despite this, ice cliffs do not compensate for the insulating effects of debris. This strongly suggests that the presence of ice cliffs is unlikely to completely counter the insulating effects of debris on other glaciers with thicker debris or lower ice cliff coverage.

### 4.2.1 *Do melt hotspots maximize melt in the ZMT?*

In order to discuss the relationship between debris, mass balance, and ice dynamics to the thinning of Kennicott Glacier we
305    must address the assumptions inherent in using the melt pattern from the summer of 2011 to represent the melt pattern over the last 60 years. At least from 2011, the surface mass balance within the zone of maximum thinning (*ZMT*) is strongly suppressed by thick debris cover. We assess what changes to our melt estimates would be required to produce the highest glacier-wide melt rates within the *ZMT*.

*Debris cover:* Debris in the *ZMT* would have to decrease to 10% of its current thickness to produce maximum glacier-wide
310    melt rates. In Part A, we noted that most of our debris thickness measurements were derived from the top of ice cliffs and topographic highs. Because debris tends to concentrate in topographic lows our debris thickness measurements may be biased toward thinner debris, making the required reduction in debris thickness even more extreme.

The *ZMT* has been continuously debris covered since at least 1957 (Fig. 12). The presence of thermokarst features, ice cliffs, and lakes in the lower 4 km of the glacier surface imply that debris greater than 5 cm was present in the *ZMT* between
315    1957 and 2009 as is the case for other debris-covered glaciers with abundant surface ponds and thermokarst features (e.g., Sakai et al., 2000; Benn et al., 2001; Wessels et al., 2002; Thompson et al., 2016). Debris cover expanded upglacier by 1.6 km between 1957 and 2009, but upglacier from the *ZMT* (Figs. 2 and 12). This suggests that sub-debris melt did not control the location of the *ZMT*.

*Ice cliffs*: In order for ice cliffs, in the *ZMT*, to enhance melt and produce maximum glacier-wide melt rates in the *ZMT*,
320    backwasting rates would need to be 7.5 times higher than those measured in the summer of 2011. This required backwasting rate is well beyond potential biases introduced due to the summer of 2011 having anomalously low air temperatures. Our backwasting estimates are based on repeated measurements at a single location at the top of each ice cliff. But as described in Part A maximum backwasting rates across each ice cliff are likely to occur near the top (Buri et al., 2016). Applying our measurements across single ice cliffs or the entire ice cliff population may therefore overestimate ice cliff melt. The

10

325  hypothetical backwasting rates required to maximize melt in the *ZMT* are therefore unreasonable; a compilation of previously published backwasting rates shown in Part A and Table 3 support this.

In order for ice cliffs in the *ZMT* to compensate for the insulating effects of debris and enhance melt in the *ZMT* beyond bare ice melt rates, ice cliff area would need to increase from 11.7% to 90% of the glacier surface. While aerial photos from the summers of 1957 and 1978 reveal an anecdotal increase in exposed ice (Fig. 12), at the upper end of the *ZMT*, far less
330  than 90% of the glacier surface was occupied by ice or ice cliffs. This suggests that ice cliff melt did not solely control the location of the *ZMT*.

*Surface lakes*: Figure 11 shows that in both 1957 and 2009 lakes are most abundant near the terminus and immediately downglacier from the *ZMT*. Surface lakes and thermokarst depressions do not coincide with the full extent of the *ZMT* and are most notably absent in its upper reaches (Fig. 11; Rickman and Rosenkrans,1997). Mass loss beneath lakes surfaces in
335  the *ZMT* would have to be 190-times the local sub-debris melt rate for sub-aqueous melt to compensate for the insulating effects of debris in the *ZMT*. This further suggests that sub-aqueous melt under lake surfaces is unlikely to compensate for the insulating effect of thick debris.

But the mottled nature of the thinning pattern in the *ZMT* highlights the melt-enhancing effects of melt hotspots. The patches of most rapid thinning occur near the 2015 glacier margin which are bordered by alluvial-bedded streams and ice
340  cliffs. While the local effect of these processes is apparent in the thinning map, it is unclear how thermokarst, surface lakes, and ice-marginal streams enhance melt outside of the hotspots themselves.

**4.3 Østrem's curve expressed in the mass balance profile**

Debris tends to thicken towards debris-covered glacier termini as is the case for Kennicott Glacier (e.g., Anderson and Anderson, 2018). This leads to the expectation that sub-debris melt rates will decline towards the terminus. At least on
345  Kennicott Glacier it appears that melt hotspots do not compensate for the melt-insulating effects of thick debris. Figure 10 shows this Østrem's curve like pattern. The low melt, low melt gradient portion of the mass balance profile extends further than the high melt high-melt gradient portion of the mass balance profile. Similar theoretical expressions of this mass balance profile can be seen in the numerical simulations presented in Anderson and Anderson (2016).

350  **5 Conclusions**

Our new ice cliff delineation method using high-resolution satellite imagery reveals that Kennicott Glacier supports the highest percentage of ice cliffs (11.7%) of any debris-covered glacier studied to date. Ice cliffs within the debris-covered portion of Kennicott Glacier partly counters the insulating effect of debris. Approximately 19% of melt in the study area is attributable to ice cliffs. In the lowest 4 kilometers of Kennicott Glacier, debris is thick, ice cliff coverage is low, but ice
355  cliffs still contribute up to 40 % of mass loss in this area. Ice cliffs contribute a larger percentage of mass loss within thicker debris covers, a trend that can be seen across the Kennicott Glacier and for other studied glaciers.

The zone of maximum thinning of Kennicott Glacier has been continuously debris-covered since at least 1957. Debris cover in the interior of the glacier expanded upglacier from 1957 to 2009. From 1957 to 2009 surface lakes have expanded

11

360    upglacier and almost doubled their areal coverage in the debris-covered portion of the glacier (see Rickman and
Rosenkrans, 1997). But lakes are not extensive enough to solely control the location of maximum thinning.

It appears that melt hotspots (ice cliffs and surface lakes) are unable to compensate for the insulating effects of thick debris
cover on Kennicott Glacier. This suggests that, in addition to melt hotspots, ice dynamics and the decline in ice discharge
from upglacier has played an important role in the thinning of the glacier under thick debris. The mass balance profile
within the debris covered portion of the glacier appears to follow Østrem's curve (the debris thickness-melt relationship). In

365    Part C we explore feedbacks that help define the rapid thinning of Kennicott Glacier under thick debris.


**Data availability**

Datasets and results are available upon request.


370    **Author contribution statement**

LSA designed the study, composed the manuscript, and all analyses besides the ice cliff delineation method. WHA
developed the ice cliff delineation method and wrote the associated text. RSA advised LSA and WHA through the study and
contributed to the text and figures. PB added important discussion that improved the manuscript. All authors revised the
manuscript.

375    **Competing Interests**

The authors declare that they have no conflict of interest.

390

## 395 References

Agarwal, V., Bolch, T., Syed, T. H., Pieczonka, T., Strozzi, T. and Nagaich, R.: Area and mass changes of Siachen Glacier (East Karakoram), Journal of Glaciology, 63(237), 148–163, doi:10.1017/jog.2016.127, 2017.

Anderson, L. S. and Anderson, R. S.: Modeling debris-covered glaciers: response to steady debris deposition, The Cryosphere, 10(3), 1105–1124, doi:10.5194/tc-10-1105-2016, 2016.

Anderson, L. S. and Anderson, R. S.: Debris thickness patterns on debris-covered glaciers, Geomorphology, 311, 1–12, doi:10.1016/j.geomorph.2018.03.014, 2018.

Anderson, R. S.: A model of ablation-dominated medial moraines and the generation of debris-mantled glacier snouts, Journal of Glaciology, 46(154), 459–469, doi:10.3189/172756500781833025, 2000.

Armstrong, W. H., Anderson, R. S. and Fahnestock, M. A.: Spatial Patterns of Summer Speedup on South Central Alaska Glaciers: Patterns of Glacier Summer Speedup, Geophysical Research Letters, 44(18), 9379–9388, doi:10.1002/2017GL074370, 2017.

Benn, D. I., Wiseman, S. and Hands, K. A.: Growth and drainage of supraglacial lakes on debris-mantled Ngozumpa Glacier, Khumbu Himal, Nepal, Journal of Glaciology, 47(159), 626–638, doi:10.3189/172756501781831729, 2001.

Brun, F., Wagnon, P., Berthier, E., Shea, J. M., Immerzeel, W. W., Kraaijenbrink, P. D. A., Vincent, C., Reverchon, C., Shrestha, D. and Arnaud, Y.: Ice cliff contribution to the tongue-wide ablation of Changri Nup Glacier, Nepal, central Himalaya, The Cryosphere, 12(11), 3439–3457, doi:10.5194/tc-12-3439-2018, 2018.

Buri, P. and Pellicciotti, F.: Aspect controls the survival of ice cliffs on debris-covered glaciers, Proceedings of the National Academy of Sciences, 115(17), 4369–4374, doi:10.1073/pnas.1713892115, 2018.

Buri, P., Pellicciotti, F., Steiner, J. F., Miles, E. S. and Immerzeel, W. W.: A grid-based model of backwasting of supraglacial ice cliffs on debris-covered glaciers, Annals of Glaciology, 57(71), 199–211, doi:10.3189/2016AoG71A059, 2016.

Das, I., Hock, R., Berthier, E. and Lingle, C. S.: 21st-century increase in glacier mass loss in the Wrangell Mountains, Alaska, USA, from airborne laser altimetry and satellite stereo imagery, Journal of Glaciology, 60(220), 283–293, doi:10.3189/2014JoG13J119, 2014.

Dougherty, E. R.: An Introduction to Morphological Image Processing (Tutorial Texts in Optical Engineering, DC O'Shea, SPIE Optical Engineering Press, Bellingham, WA, USA, 1992.

Duan, Q., Sorooshian, S. and Gupta, V.: Effective and efficient global optimization for conceptual rainfall-runoff models, Water resources research, 28(4), 1015–1031, 1992.

Han, H., Wang, J., Wei, J. and Liu, S.: Backwasting rate on debris-covered Koxkar glacier, Tuomuer mountain, China, Journal of Glaciology, 56(196), 287–296, doi:10.3189/002214310791968430, 2010.

Herreid, S. and Pellicciotti, F.: Automated detection of ice cliffs within supraglacial debris cover, The Cryosphere, 12(5), 1811–1829, doi:10.5194/tc-12-1811-2018, 2018.

Hock, R.: Temperature index melt modelling in mountain areas, Journal of Hydrology, 282(1–4), 104–115, doi:10.1016/S0022-1694(03)00257-9, 2003.

Immerzeel, W. W., Kraaijenbrink, P. D. A., Shea, J. M., Shrestha, A. B., Pellicciotti, F., Bierkens, M. F. P. and de Jong, S. M.: High-resolution monitoring of Himalayan glacier dynamics using unmanned aerial vehicles, Remote Sensing of Environment, 150, 93–103, doi:10.1016/j.rse.2014.04.025, 2014.

Juen, M., Mayer, C., Lambrecht, A., Han, H. and Liu, S.: Impact of varying debris cover thickness on ablation: a case study for Koxkar Glacier in the Tien Shan, The Cryosphere, 8(2), 377–386, doi:10.5194/tc-8-377-2014, 2014.

Kääb, A., Berthier, E., Nuth, C., Gardelle, J. and Arnaud, Y.: Contrasting patterns of early twenty-first-century glacier mass change in the Himalayas, Nature, 488(7412), 495–498, doi:10.1038/nature11324, 2012.

Kirkbride, M. P.: The temporal significance of transitions from melting to calving termini at glaciers in the central Southern Alps of New Zealand, The Holocene, 3(3), 232–240, doi:10.1177/095968369300300305, 1993.

Lamsal, D., Fujita, K. and Sakai, A.: Surface lowering of the debris-covered area of Kanchenjunga Glacier in the eastern Nepal Himalaya since 1975, as revealed by Hexagon KH-9 and ALOS satellite observations, The Cryosphere, 11(6), 2815–2827, doi:10.5194/tc-11-2815-2017, 2017.

Leyk, S. and Boesch, R.: Colors of the past: color image segmentation in historical topographic maps based on homogeneity, GeoInformatica, 14(1), 1, 2010.

Miles, E. S., Willis, I., Buri, P., Steiner, J. F., Arnold, N. S. and Pellicciotti, F.: Surface Pond Energy Absorption Across Four Himalayan Glaciers Accounts for 1/8 of Total Catchment Ice Loss, Geophysical Research Letters, 45(19), 10,464-10,473, doi:10.1029/2018GL079678, 2018.

Mölg, N., Bolch, T., Walter, A. and Vieli, A.: Unravelling the evolution of Zmuttgletscher and its debris cover since the end of the Little Ice Age, The Cryosphere, 13(7), 1889–1909, doi:10.5194/tc-13-1889-2019, 2019.

Nuimura, T., Fujita, K., Yamaguchi, S. and Sharma, R. R.: Elevation changes of glaciers revealed by multitemporal digital elevation models calibrated by GPS survey in the Khumbu region, Nepal Himalaya, 1992-2008, Journal of Glaciology, 58(210), 648–656, doi:10.3189/2012JoG11J061, 2012.

Nye, J. F.: The response of glaciers and ice-sheets to seasonal and climatic changes, Proceedings of the Royal Society of London. Series A. Mathematical and Physical Sciences, 256(1287), 559–584, doi:10.1098/rspa.1960.0127, 1960.

Pellicciotti, F., Stephan, C., Miles, E., Herreid, S., Immerzeel, W. W. and Bolch, T.: Mass-balance changes of the debris-covered glaciers in the Langtang Himal, Nepal, from 1974 to 1999, Journal of Glaciology, 61(226), 373–386, doi:10.3189/2015JoG13J237, 2015.

Porter, C., Morin, P., Howat, I., Noh, M.-J., Bates, B., Peterman, K., Keesey, S., Schlenk, M., Gardiner, J., Tomko, K., Willis, M., Kelleher, C., Cloutier, M., Husby, E., Foga, S., Nakamura, H., Platson, M., Wethington, M., Jr., Williamson, C., Bauer, G., Enos, J., Arnold, G., Kramer, W., Becker, P., Doshi, A., D'Souza, C., Cummens, P., Laurier, F. and Bojesen, M.: ArcticDEM, , doi:10.7910/DVN/OHHUKH, 2018.

Reed, P. M., Hadka, D., Herman, J. D., Kasprzyk, J. R. and Kollat, J. B.: Evolutionary multiobjective optimization in water resources: The past, present, and future, Advances in water resources, 51, 438–456, 2013.

Reid, T. D. and Brock, B. W.: Assessing ice-cliff backwasting and its contribution to total ablation of debris-covered Miage glacier, Mont Blanc massif, Italy, Journal of Glaciology, 60(219), 3–13, doi:10.3189/2014JoG13J045, 2014.

Richards, J. A.: Remote Sensing Digital Image Analysis, Fifth., Springer-Verlag, Berlin., 2013.

Rickman, R. L. and Rosenkrans, D. S.: Hydrologic Conditions and Hazards in the Kennicott River Basin, Wrangell-St. Elias National Park and Preserve, Alaska, Water-Resources Investigations Report, U.S. Geological Survey, Anchorage, Alaska., 1997.

Sakai, A., Takeuchi, N., Fujita, K. and Nakawo, M.: Role of supraglacial ponds in the ablation process of a debris-covered glacier in the Nepal Himalayas, in Debris-Covered Glaciers, vol. 265, p. 12, IAHS, Seattle, Washington., 2000.

Sakai, A., Nakawo, M. and Fujita, K.: Distribution Characteristics and Energy Balance of Ice Cliffs on Debris-covered Glaciers, Nepal Himalaya, Arctic, Antarctic, and Alpine Research, 34(1), 12–19, doi:10.1080/15230430.2002.12003463, 2002.

Sauvola, J. and Pietikäinen, M.: Adaptive document image binarization, Pattern Recognition, 33(2), 225–236, doi:10.1016/S0031-3203(99)00055-2, 2000.

Shean, D. E., Alexandrov, O., Moratto, Z. M., Smith, B. E., Joughin, I. R., Porter, C. and Morin, P.: An automated, open-source pipeline for mass production of digital elevation models (DEMs) from very-high-resolution commercial stereo satellite imagery, ISPRS Journal of Photogrammetry and Remote Sensing, 116, 101–117, 2016.

Steiner, J. F., Pellicciotti, F., Buri, P., Miles, E. S., Immerzeel, W. W. and Reid, T. D.: Modelling ice-cliff backwasting on a debris-covered glacier in the Nepalese Himalaya, Journal of Glaciology, 61(229), 889–907, doi:10.3189/2015JoG14J194, 2015.

Thompson, S., Benn, D. I., Mertes, J. and Luckman, A.: Stagnation and mass loss on a Himalayan debris-covered glacier: processes, patterns and rates, Journal of Glaciology, 62(233), 467–485, doi:10.1017/jog.2016.37, 2016.

Vincent, C., Wagnon, P., Shea, J., Immerzeel, W., Kraaijenbrink, P., Shrestha, D., Soruco, A., Arnaud, Y., Brun, F., Berthier, E. and Sherpa, S.: Reduced melt on debris-covered glaciers: investigations from Changri Nup Glacier, Nepal, The Cryosphere, 15, 2016.

Watson, C. S., Quincey, D. J., Smith, M. W., Carrivick, J. L., Rowan, A. V. and James, M. R.: Quantifying ice cliff evolution with multi-temporal point clouds on the debris-covered Khumbu Glacier, Nepal, Journal of Glaciology, 63(241), 823–837, doi:10.1017/jog.2017.47, 2017.

Wessels, R. L., Kargel, J. S. and Kieffer, H. H.: ASTER measurement of supraglacial lakes in the Mount Everest region of the Himalaya, Annals of Glaciology, 34, 399–408, doi:10.3189/172756402781817545, 2002.

Wu, K., Liu, S., Jiang, Z., Xu, J., Wei, J. and Guo, W.: Recent glacier mass balance and area changes in the Kangri Karpo Mountains from DEMs and glacier inventories, The Cryosphere, 12(1), 103–121, doi:10.5194/tc-12-103-2018, 2018.

Yapo, P. O., Gupta, H. V. and Sorooshian, S.: Multi-objective global optimization for hydrologic models, Journal of hydrology, 204(1–4), 83–97, 1998.

400

**Tables**

**Table 1.** Optimal image processing parameters for ice cliff delineation in the July 2009 WorldView scene, as determined by a Monte Carlo method.

| Adaptive binary threshold (ABT) | Min brightness [DN*] | Max brightness [DN] | Window size [px] | Brightness offset [DN] | Opening kernel size [px] |
|---|---|---|---|---|---|
| | 20 | 42 | 267 | 52 | 3 |

| Sobel edge detection (SED) | Min brightness [DN] | Max brightness [DN] | Threshold gradient [DN px⁻¹] | Opening kernel size [px] | |
|---|---|---|---|---|---|
| | 32 | 55 | 22 | 4 | |

*DN = digital number, a 0-255 representation of relative radiance of each pixel.

405

**Table 2.** Parameters used for distributed melt estimates

| Parameter name | Parameter symbol | Most-likely | Min. | Max. |
|---|---|---|---|---|
| Debris thickness ($h_{debris}$) [cm] | a | 25.7 | 20.5 | 40.2 |
| | b | 571 | 545 | 607 |
| | c | -0.24 | -0.15 | -5.3 |
| Sub-debris ablation [cm d⁻¹] | $\dot{b}_{ice}$ | 5.87 | 4.87 | 6.87 |
| | $h_{star}$ | 8.17 | 8.17 | 8.17 |
| Ice cliff backwasting [cm d⁻¹] | f | -0.0123 | -0.0079 | -0.0111 |
| | g | 13.94 | 10.25 | 15.11 |
| Ice cliff slope [degree] | θ | 40 | 30 | 50 |
| Ice cliff area (%) | - | 11.7 | 9.7 | 11.7 |

410

16

The Cryosphere
Discussions

Open Access

EGU

**Table 3.** Comparison of ice cliff coverage and melt contribution on debris-covered glaciers

| Glacier | Ice cliff fractional area (%) | Ice cliff mass loss (%) | Mean debris thickness [cm] | Study |
|---|---|---|---|---|
| Ngozumpa, Nepal | 5 | 40 | 0-300 | (Thompson et al., 2016) |
| Lirung, Nepal | 2.0 | 36 | 50-100 | (Buri and Pellicciotti, 2018) |
| Changri Nup, Nepal | 7.4 | 24 (±5) | - | (Brun et al., 2018) |
| Langtang, Nepal | 1.3 | 20 | - | (Buri and Pellicciotti, 2018) |
| Kennicott, Alaska | 11.6 | 19 (±8) | 13 | This study |
| Koxkar, China | 1.4 | 7.4-12 | 53 | (Han et al., 2010; Juen et al., 2014) |
| Miage, Italy | 1.3 | 7.4 | 26 | Reid and Brock (2014) |

415    **EB refers to energy balance

420

425

430

435

440

445

17
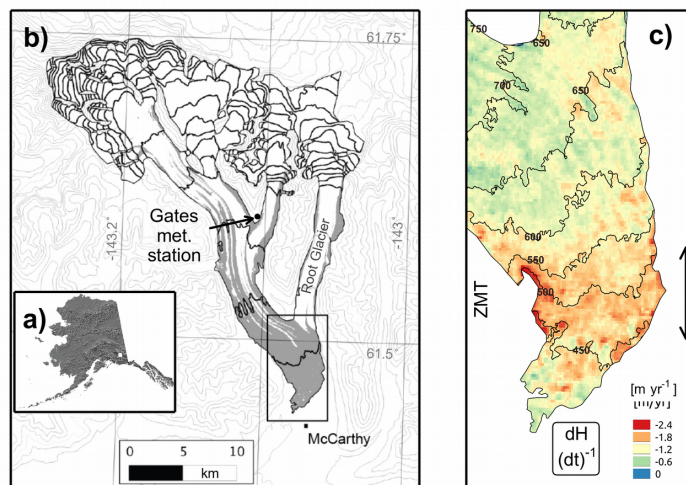
**Figures**



**Figure 1.** Map of Kennicott Glacier and the study area. a) Map of Alaska showing the location of panel b and the Wrangell Mountains. b) The Kennicott Glacier with the location of the Gates glacier meteorological station (1240 m a.s.l.). c) Map of the study area (24.2 km$^2$) with dH (dt)$^{-1}$ from 1957 to 2009 see Das et al. (2014) (mean error 0.04 m yr$^{-1}$ and 1 std 0.15 m yr$^{-1}$ based on 3 km$^2$ area within 4 km of the modern terminus). *ZMT* refers to the zone of maximum thinning, the extent of which is shown with the double-headed arrow.

450

455

460
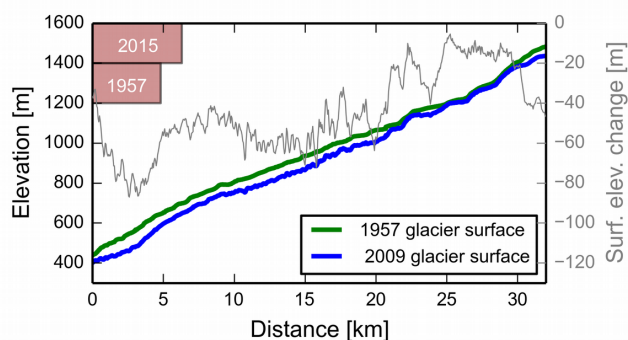
**Figure 2.** Glacier surface elevation change between 1957 and 2009. Surface elevation profiles from USGS DEM (1957) and the ASTER GDEM V2 (2009) along a swath profile following the centerline of the Kennicott Glacier. The greatest change in glacier surface elevation occurs within the portion of the glacier where debris spans the glacier width continuously between 1957 and 2009. Note the topographic bulge in the 2009 profile at the upper end of the zone of maximum thinning. Note the substantial thinning that has occurred upglacier from the continuous debris cover.

465

470
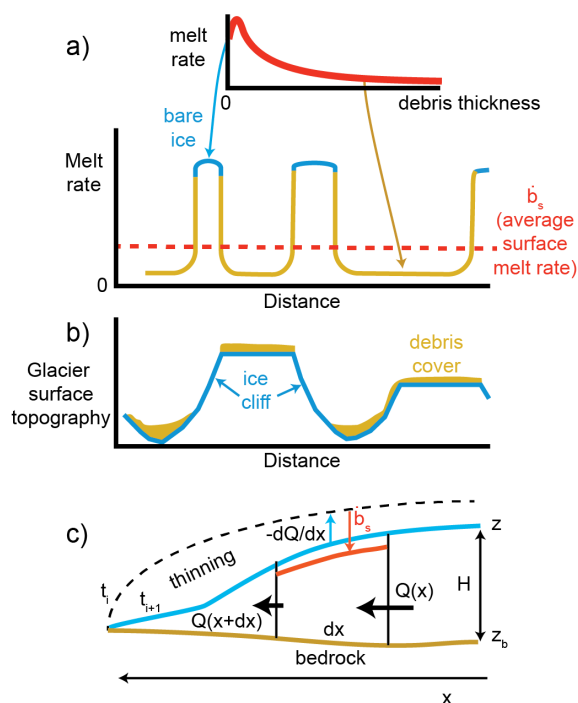
**Figure 3.** Schematic comparing the relative roles of ice cliff backwasting, sub-debris melt, and ice surface uplift (ice emergence rate) to the lowering of an idealized Kennicott Glacier terminus. a) Idealized relationship between ice cliff backwasting and sub-debris melt. Noting that the inclined facing and low albedo of ice cliffs can lead to melt rates that exceed bare ice melt rates on a flat surface. b) Glacier surface topography with debris cover and ice cliffs compared to melt rates in panel a. c) Schematic showing the relationship between surface melt, ice dynamics, and the thinning of the Kennicott Glacier through time.

475

480

20

485
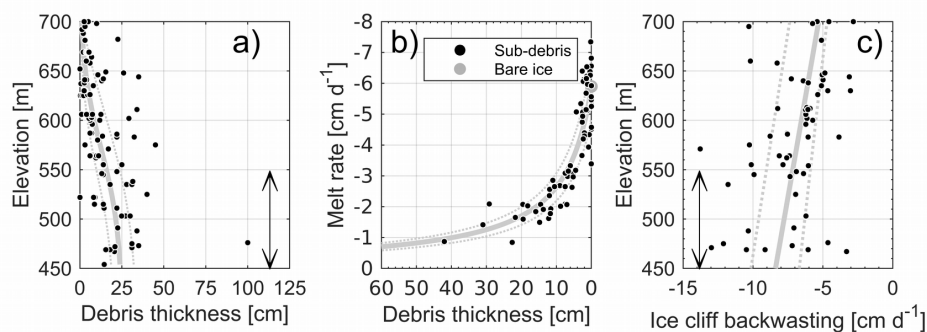


**Figure 4.** Data used to extract curve fits for the distributed melt estimate. See Part A for a full description of the methods. a) Debris thickness as it varies with elevation. The grey line is the best fit polynomial. The dashed lines are based on best fit polynomials through the 25 and 50% elevation bins. The double-headed arrow represents the zone of maximum thinning (*ZMT*). b) Melt rate as it varies with debris thickness. More negative melt is the equivalent to larger magnitude melt. The solid line is the curve-fit for the most likely ablation-debris thickness relationship. The dotted lines represent the error bounds used in the distributed estimate of melt. The axes are flipped so the orientation is consistent with other figures. c) Ice cliff backwasting rate as it varies with elevation. The solid grey line is the linear best-fit through the median of each 50 m elevation bin. The black line is the best-fit through all of the data. The dashed lines are linear fits through the 25% and 75% of each 50 m elevation bin (see Table 2 for curve fit parameters). The double-headed arrow represents the zone of maximum thinning (*ZMT*).
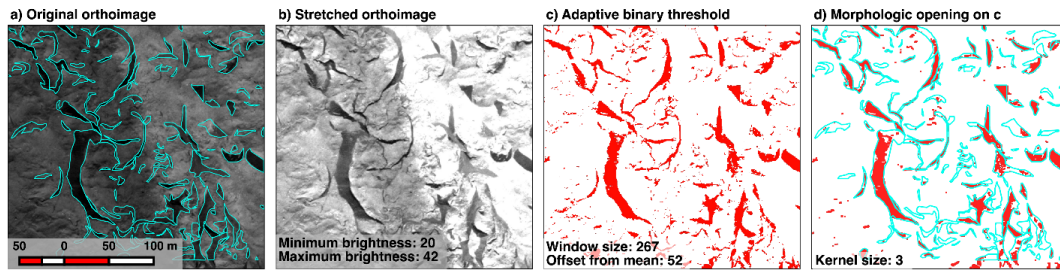
490

495

500

505

510

21

**Figure 5.** Ice cliff detection workflow for the adaptive binary threshold (*ABT*) method. a) Original orthoimage with manually digitized ice cliffs shown in cyan. b) Orthoimage after histogram stretch using a set of well-performing brightness values from the parameter optimization. c) *ABT* on stretched orthoimage. d) Morphologic opening on adaptive binary threshold to remove small isolated false positive ice cliff detections. Manually digitized ice cliffs again shown in cyan.

515

520

525

530

22
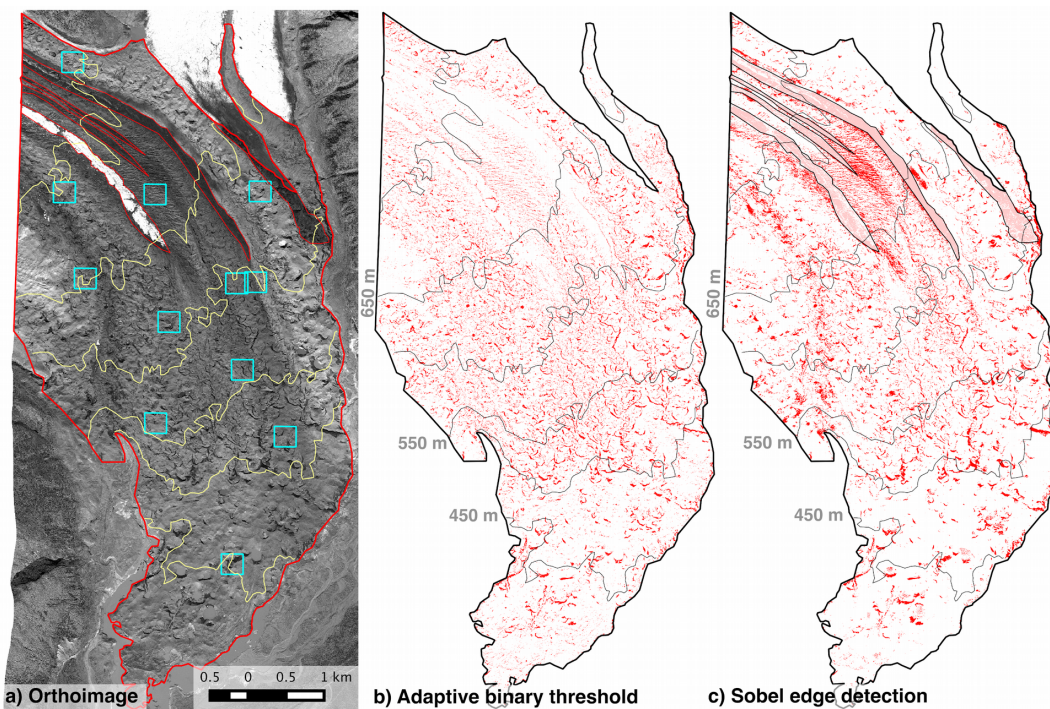
**Figure 6.** Results from the two ice cliff detection methods. a) Orthoimage of the terminus of Kennicott Glacier, with the
535   debris-covered study area outlined by the thick red line. The thin red lines show regions of dark and light bare ice that
required special treatment in the *SED* method. Thin yellow lines are elevation contours with a 50 m contour interval. Blue
boxes show the locations of manually digitized ice cliff area, used for error analysis and parameter optimization. b) Ice cliff
spatial distribution as estimated by the adaptive binary threshold (*ABT*) method, with overlaid elevation contours from 2013.
c) Ice cliff spatial distribution as estimated by the Sobel edge detection (*SED*) method, with overlaid elevation contours
540   from 2013.

23
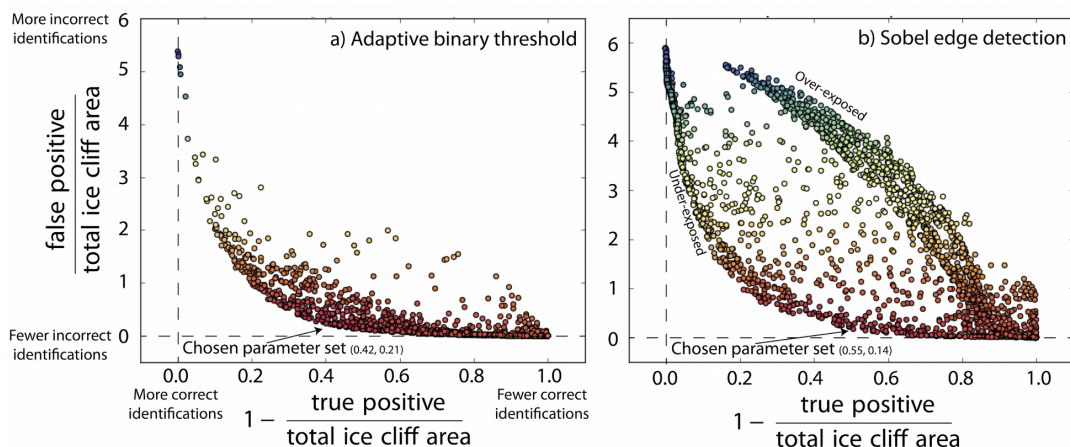
**Figure 7.** Parameter optimization for a) adaptive binary threshold (*ABT*) and b) sobel edge detection (*SED*) ice cliff detection algorithms. On each plot, every point represents algorithm ice cliff detection error averaged across twelve manually digitized zones. The horizontal axes show true positives (i.e., automated and hand-digitized ice cliffs agree) and vertical axes show false positives (i.e., automated method predicts ice cliff where none exists). Perfect algorithm performance would plot on the origin. The coordinates for our chosen parameter sets provide an estimate of the error associated with the method. Note the differing axis limits on the horizontal and vertical axes. Markers are colored by Euclidean distance from the origin.

24
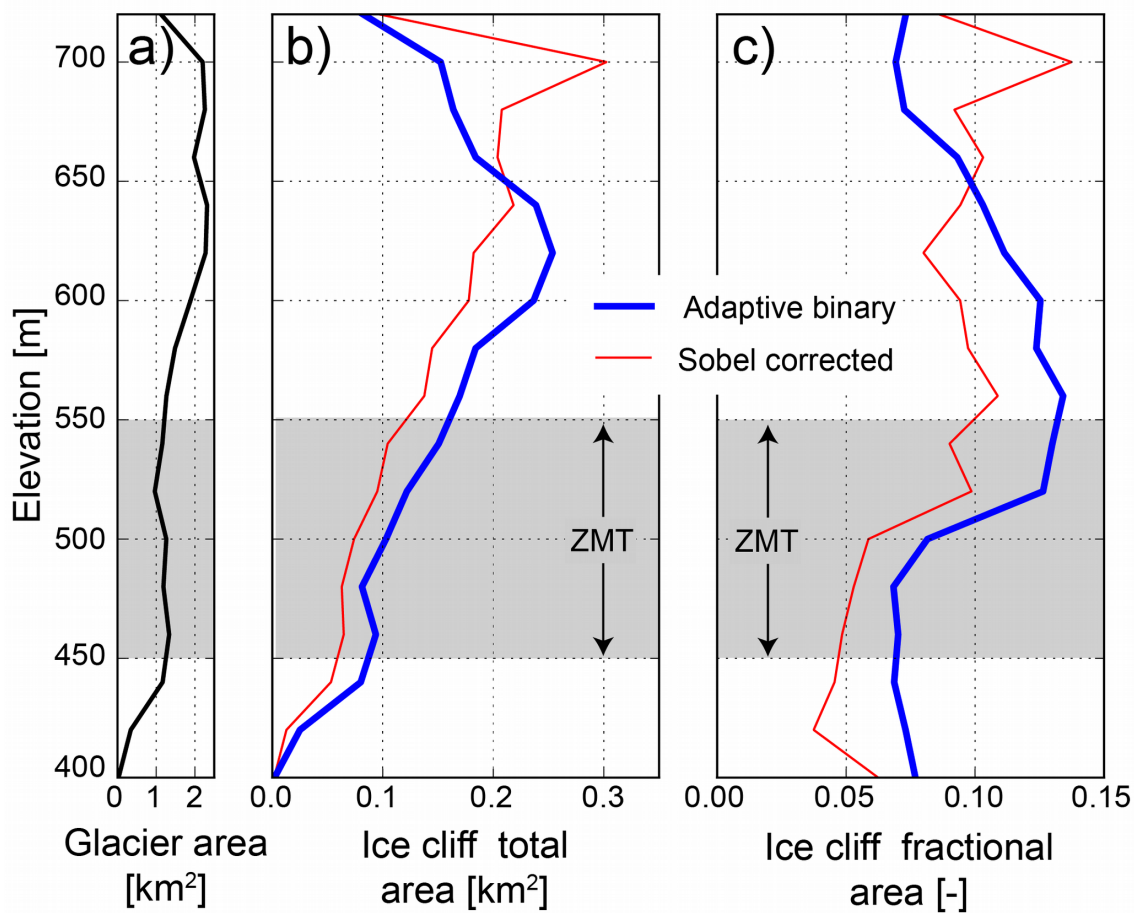
**Figure 8.** Results from the two ice cliff detection methods with elevation. a) Glacier area as a function of elevation. b) Ice cliff area as a function of elevation. The red line shows results from the *SED* approach after false positives on dark colored ice are removed. c) Ice cliff area as a function of elevation, normalized by the glacier area within each elevation band.

560

25
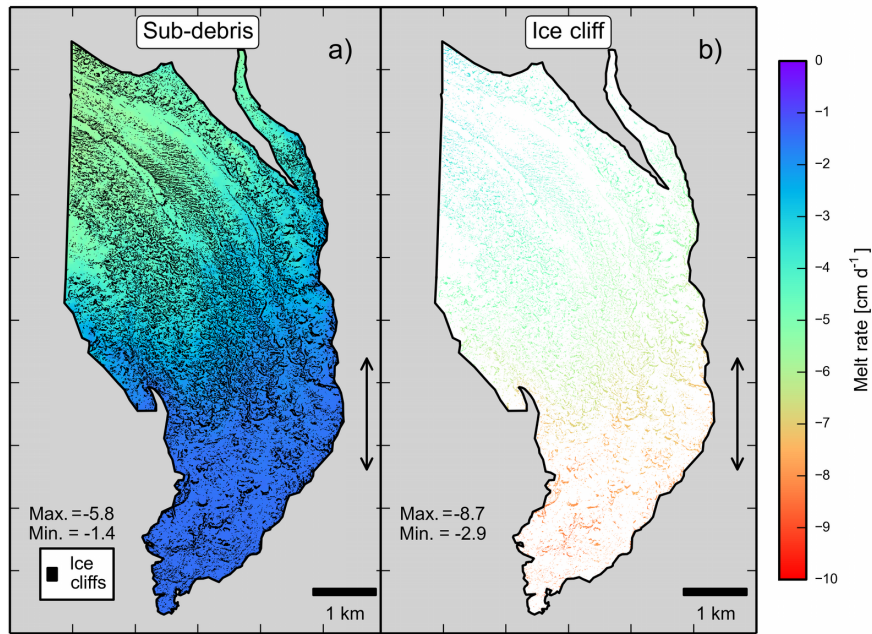
**Figure 9.** Extrapolated ablation based on elevation across the study area. The more negative number the more the melt. The zone of maximum thinning (*ZMT*) is defined by the double-headed arrows in each panel. a) Most-likely sub-debris melt rate which decreases in magnitude downglacier. b) Most-likely ice cliff backwasting rate which increases in magnitude down glacier.
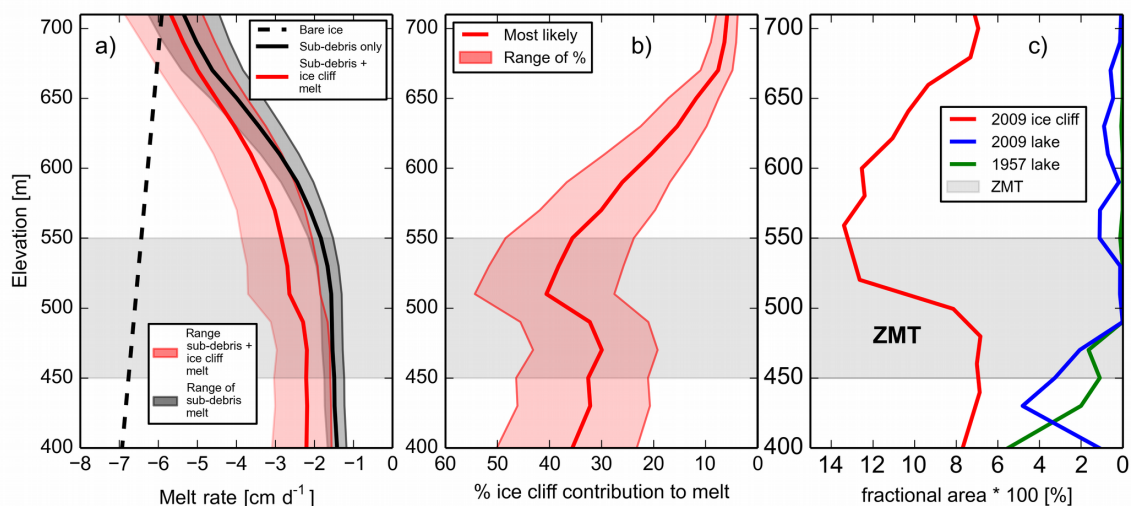
**Figure 10.** Melt-related estimates with elevation. Elevations are relative to the 2013 glacier surface. The zone of maximum thinning (*ZMT*) is represented by the grey bands for both panels. a) The elevation-band-averaged melt over the study period combining in situ measurements of ice cliff and sub-debris melt. The expected melt pattern primarily follows the shape of Østrem's curve. Bare-ice estimates are based on the near-surface air temperature lapse rate and melt factor for ice (Part A). The more negative the number the more the magnitude of melt. b) The percent contribution of ice cliffs to mass loss (sub-debris + ice cliff) with elevation. c) The fractional area of ice cliffs, and surface lakes. Note that the fractional area of ice cliff coverage maximizes and surface lake coverage minimizes in the upper portion of the *ZMT* (see Part C).

565

570

575

580
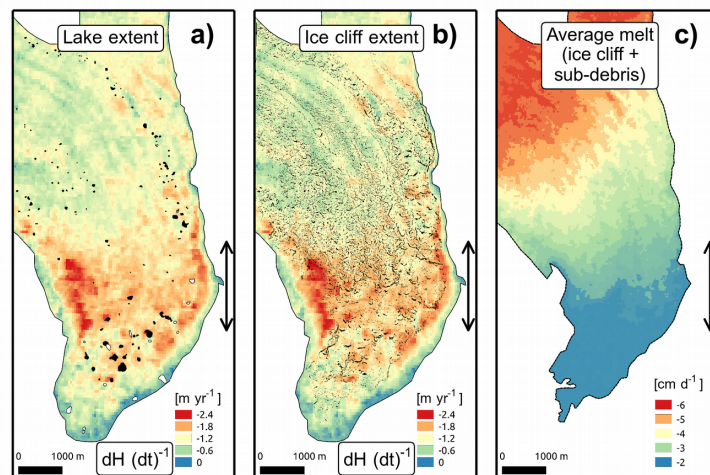
**Figure 11.** Comparison ice cliff and lake extent with the *ZMT* and estimated melt rates. a) Glacier surface lowering and surface lake extent. Observed surface lakes from the 1957 aerial photo are shown with white fill and black outlines. Observed surface lakes from 2009 from WV imagery are shown in black. b) Glacier surface lowering and 2009 ice cliff extent based on the *ABT* method. d) Elevation-band averaged melt due to ice cliffs and sub-debris melt from the summer of 2011.

28
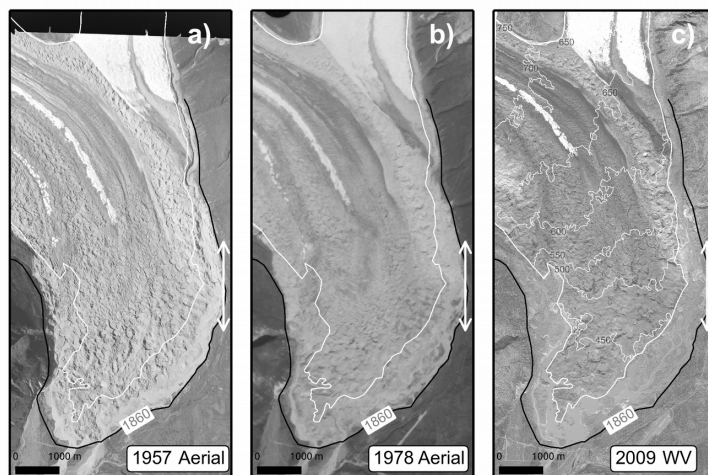
**Figure 12.** Aerial imagery of the study area from 1957, 1978, and 2009. Imagery of the Kennicott Glacier from 1957, 1978, and 2009, showing changes in the glacier surface through time. The arrows show the zone of maximum thinning (*ZMT*) between 1957 and 2009. The *ZMT* has been continuously debris covered since at least 1957. a) Aerial photo from July 29 1957 (courtesy of the USGS). b) Aerial photo from 25 August 1978 (courtesy of the USGS). The darkening of the glacier surface on the western portion of the glacier in the 1978 image may represent an increase in ice cliffs or a change in illumination angle. c) WorldView image from 13 July 2009. Note the expansion of debris upglacier in time.